INSTITUTE OF PHYSICS PUBLISHING JOURNAL OF PHYSICS: CONDENSED MATTER

J. Phys.: Condens. Matter **17** (2005) 7061–7075 doi:10.1088/0953-8984/17/43/022

In situ small-angle neutron scattering investigation of the γ' precipitation and growth in the nickel-based single-crystal alloy SC16

N Ratel[1], **G Bruno**[1,2,3] **and B Demé**[1]

[1] Institut Laue Langevin-6, rue Jules Horowitz-BP 156-38042, Grenoble Cedex 9, France
[2] Manchester Materials Science Centre, School of Materials, University of Manchester, Grosvenor Street, Manchester M1 7HS, UK

E-mail: bruno@ill.fr

Received 20 June 2005, in final form 20 September 2005
Published 14 October 2005
Online at stacks.iop.org/JPhysCM/17/7061

Abstract

The precipitation of γ' particles in the SC16 single-crystal nickel-based superalloy has been studied by *in situ* small-angle neutron scattering (SANS). On cooling from the one-phase field γ (temperatures above 1250 °C), the γ' precipitates develop in different sizes and shapes at each temperature. Samples underwent solutionizing and different ageing treatments below the solutionizing point in a saw-tooth temperature profile. Microstructural information, as well as relative volume fraction and size of the particles, could be deduced from SANS patterns at each ageing temperature. They indirectly show that the precipitates have a cuboidal shape and are arranged (periodically) along the [100] crystallographic direction, only at temperatures below 1180 °C. Between 1180 and 1120 °C the transition from spherical to cuboidal shape seems to take place, driven by the prevalence of the strain energy over the other driving mechanisms of the reaction. More than one particle population is necessary to interpret the scattering profiles at each temperature. Nucleation of small particles seems to take place down to 1050 °C. Morphology evolutions as a function of temperature as well as possible splitting of the precipitates are discussed.

1. Introduction

The development from polycrystalline to single-crystal turbine parts has led to an improvement of the mechanical properties and an increase of the operating temperature of nickel-based superalloys. The peculiar properties of these single-crystal alloys come from a precipitate phase, named γ', whose crystal structure is fcc, like the γ matrix in which they are embedded,

[3] Author to whom any correspondence should be addressed.

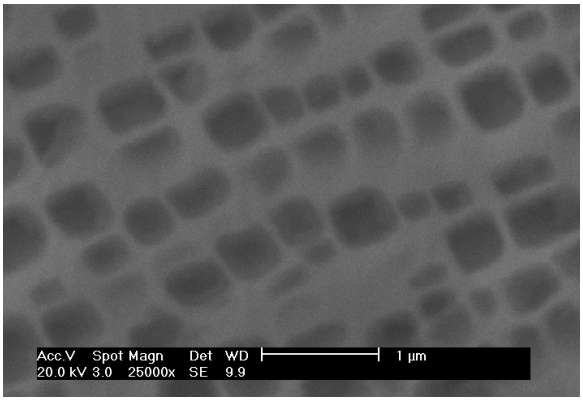

Figure 1. An example of the cuboidal precipitate microstructure of Ni-based superalloy SC16 after standard heat treatment (TEM dark-field image).

Table 1. Composition of the SC16 superalloy.

Element	Ni	Al	Ti	Ta	Cr	Mo
At.%	68.1	7.35	4.15	1.1	17.5	1.8

but with $L1_2$ structure corresponding to a chemical order $Ni_3(Al, Ti)$. A very high shear resistance at high temperature is accompanied by an increase of the flow stress around 800 °C (as opposed to usual alloys like steels) because of the formation and interaction of complex stacking faults [1]. The mechanical properties of these materials strongly depend on the morphology of the precipitates and of their volume fraction [2].

The superalloy SC16 belongs to the first generation of single-crystal materials for stationary turbines with low γ' volume fraction (about 40%). Its composition is given in table 1. Although more advanced alloys have been developed, which contain heavy refractory elements, the low number of compositional elements in SC16 gives the advantage of an easier modelling of the diffusion properties. After standard heat treatment (SHT) of the original material (1250 °C /3 h/water quenched+1100 °C/1 h/air cooling+850 °C/24 h/air cooling), the microstructure of SC16 consists of large γ' cuboids (usually about 400–500 nm edge) oriented with the edges parallel to the $\langle 001 \rangle$ crystallographic direction and surrounded by γ matrix channels, as shown in figure 1.

On cooling from the one-phase field γ, there will be a critical temperature, below which the γ' particles start building up. Indeed, there are three variables which drive the γ' precipitation reaction: the difference of free enthalpy of the phases per unit volume $\Delta g_{\gamma\gamma'}$, the particle/matrix interfacial energy $f_{\gamma\gamma'}$ and the elastic strain energy due to lattice mismatch between precipitate and matrix and due to overlapping of strain fields $\Delta g^{\varepsilon}_{\gamma\gamma'}$ [2]. Therefore, the variation of the Gibbs energy necessary for the formation of the particles, $\Delta G_{\gamma\gamma'}$, is given by [3]:

$$\Delta G_{\gamma\gamma'} = -V_{\gamma'} \cdot \Delta g_{\gamma\gamma'} + F_{\gamma'} f_{\gamma\gamma'} + V_{\gamma'} \Delta g^{\varepsilon}_{\gamma\gamma'} \tag{1}$$

where $V_{\gamma'}$ is the volume occupied by the particles and $F_{\gamma'}$ the particle/matrix interfacial area.

The prevalence of the interfacial energy over the elastic strain energy in equation (1) determines the character of the reaction (respectively diffusion or strain driven) as well as the morphology and the size of the γ' precipitates. Growth and coarsening of the precipitates take place at any temperature below the critical undercooling (about 30 °C below the solvus point). This result has been predicted by Cahn [4] and confirmed by Bruno and Pinto [5].

Coarsening is described by the Ostwald ripening (see the works of Lifshitz and Slyozov [6] and Wagner [7]—the LSW theory). Khachaturyan *et al* [8, 9] developed a theoretical analysis to model morphological changes occurring during coarsening of cubic precipitates. Their model implies that, as the particles grow beyond a certain size, they split into smaller particles and/or change their form, due to the effects of elastic interaction. The following morphological shape transitions were predicted: sphere → cube → doublet → octet → platelet. Yamabe and Harada [10] explained particle splitting in terms of chemical composition fluctuation from the equilibrium state.

Up to now there are very few works monitoring *in situ* the nucleation and growth of the γ' phase in technical alloys such as SC16. Hopgood and Martin [11] observed the coarsening of γ' in the alloy SRR 99 as a function of the ageing time at fixed temperatures by means of transmission electron microscopy (TEM). Royer *et al* [12] investigated by scanning electron microscopy (SEM) and TEM the change in morphology during the rafting of the particles in the AM1 superalloy, but still starting from room temperature (RT) and approaching the solvus temperature from below. A similar approach was used in a SANS study [13] where the morphology of precipitates below the solutionizing temperature of Re-rich Ni-based superalloy (Re13) was investigated. Malow *et al* [14, 15] studied the effect of the solutionizing, but still using heat-treated TEM samples, investigated at RT. Gilles *et al* [16, 17] used SANS combined with TEM and SEM investigations to characterize the microstructure of SC16, again measuring water-quenched samples. Ricks *et al* [18] report the growth of γ' dendrites in the $\langle 111 \rangle$ directions, and Westbrook [19] reports the phenomenon as growth + splitting of Ni_3Al particles embedded in a Ni-based alloy in an ogdoadical [20] form. Again, the latter base their analysis on TEM results.

While TEM provides mainly 'local' information, frequently making difficult the determination of the bulk volume fraction with accuracy, SANS provides bulk averaged information on the parameters of the microstructure (i.e., precipitate morphology, distance between precipitates as well as volume fraction). Moreover, TEM is usually believed to show the additional precipitation of very fine γ' particles that may occur during quenching. If used *in situ*, SANS is a powerful tool to tackle problems like the observation of the early stages of the precipitation in single-crystal alloys [20]. Therefore, *in situ* SANS studies were used in this work to follow the evolution of the precipitates morphology as a function of temperature and time.

2. Experimental procedure

Three (virtually identical) samples (size $15 \times 10 \times 2$ mm^3, cut from the same as-cast ingot) were pre-oriented by the Laue x-ray scattering technique with one face perpendicular to the [001] crystal direction. The sample surface normal was aligned parallel to the neutron beam. The SANS experiment was carried out on the D11 pinhole camera at the ILL (Grenoble, France), equipped with a two-dimensional position-sensitive detector (PSD) and an induction furnace (standard ILL-type high-temperature furnace with a ceramic sample holder). The neutron wavelength used was $\lambda = 6$ Å. Table 2 summarizes the three experimental set-ups used, which correspond to three complementary q-ranges (where q is the scattering vector modulus).

Each sample was measured in only one instrumental set-up, but the same temporal saw-tooth temperature profile (shown in figure 2) was applied to all. The samples were heated up to the solutionizing point (1250 °C), held for 2–3 h to ensure that the γ' phase disappeared and then aged at certain temperatures for 1–2 h. This cycle was repeated several times, changing the ageing temperature. The temperatures chosen were 1220, 1180, 1120, 1050, 860 °C and

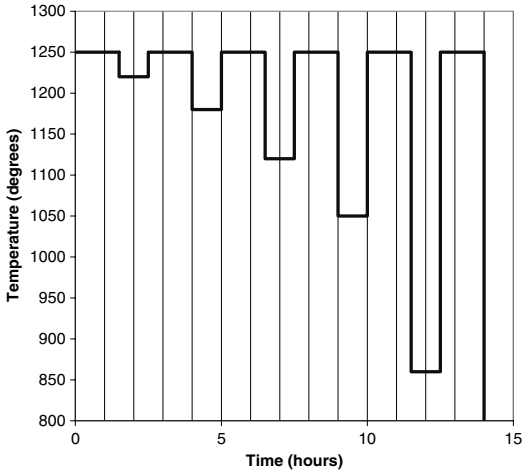

Figure 2. Temperature profile applied to each sample (i.e., each experimental set-up, see text) during the experiment.

Table 2. Instrument set-up for this investigation. D_{sd} is the sample to detector distance.

Sample	D_{sd} (m)	Collimation (m)	q_{min} (Å^{-1})	q_{max} (Å^{-1})
1	2.5	2.5	2.42×10^{-2}	1.54×10^{-1}
2	5.5	5.5	1.13×10^{-2}	6.85×10^{-2}
3	20	20.5	2.31×10^{-3}	1.74×10^{-2}

RT. Each sample was previously oriented so that the beam direction was nearly parallel to the [001] crystallographic axis. The SANS data were treated using the GRASP software developed at the ILL [21]. Corrections for background, solid angle viewed by a pixel on the PSD, sample transmission, cell transmission and cadmium were taken into account, but no water and/or vanadium measurement for absolute normalization of the data was carried out, because only relative differences with respect to the pure γ phase were investigated and relevant.

3. Results

Figure 3 shows some typical examples of SANS patterns obtained. Essentially, we observed that for a temperature range between 1180 and 1250 °C, the SANS pattern was isotropic (figure 3(a)), which is representative of spherical particles. For temperatures below 1120 °C, the SANS patterns looked anisotropic with a fourfold symmetry, typical of a periodical arrangement of cuboidal γ' precipitates along the [100] direction [22]. No calibration measurement (water or vanadium) was carried out, because the results only need to be compared relatively to those obtained at 1250 °C, when theoretically all the γ' precipitates are dissolved [14]. Therefore intensity data will be represented in arbitrary units in the following. This does not undermine any of the conclusions drawn in this work. In the case of isotropic patterns, data were azimuthally averaged so as to obtain the 1D scattering curve $I(q)$. In the case of anisotropic patterns, data were averaged azimuthally and along specific directions such as [100], [010] and [110]. Anisotropic SANS patterns as well as the integration sectors are shown in figures 3(b)–(d). In the q-range investigated, we did not observe interference maxima, so no conclusion about the particle periodicity could be drawn.

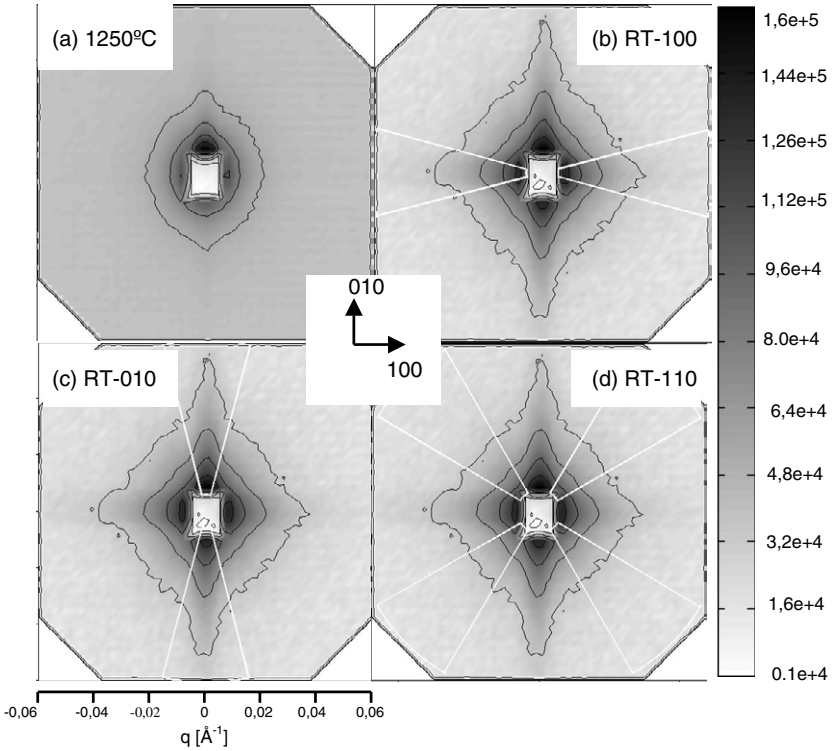

Figure 3. (a) Isotropic SANS pattern obtained at 1250 °C azimuthally averaged; (b) averaging of an anisotropic SANS pattern obtained at RT along the [100] direction; (c) averaging along the [010] direction (same data as (b)); (d) averaging along the [110] direction. The sectors for the directional analyses have a 30° aperture angle.

The cuboidal form of the γ' phase in a Re-rich Ni-based superalloy was observed to be kept up to the solvus temperature [23]. In the present experiment, it has been found that the cubic microstructure and the alignment along the $\langle 100 \rangle$ directions build up only at temperatures below 1180 °C. This difference can be attributed to the following.

(a) The fact that the temperature profile was taken in opposite directions: the *solvus* temperature was approached from below, while we dissolved all the precipitates above the *solvus* point and then decreased the temperature. Starting from RT [23], the order is more difficult to lose and the precipitates can keep their cuboidal form.
(b) The different composition, which leads to higher solutionizing temperatures for a Re-rich alloy (∼1300 °C). This implies a different temperature scale for the two alloys.
(c) The smaller misfit at high temperature for SC16 with respect to the alloy investigated in [23]. This determines a 'more spherical' shape of the precipitates.
(d) The main contribution to the scattering at very high temperatures comes also from other particles than γ': micropores and/or TCP phases which were not dissolved during homogenization or dissolve only very slowly [14] (see section 4.1).

As mentioned before, each sample was kept at a certain temperature for about one hour but SANS patterns were recorded every ten minutes. The possibility of a kinetic study of the γ' precipitation was checked by comparing the evolution of the 1D scattering curves with time at a given temperature. As shown in an example (figure 4), no evolution of the scattered intensity

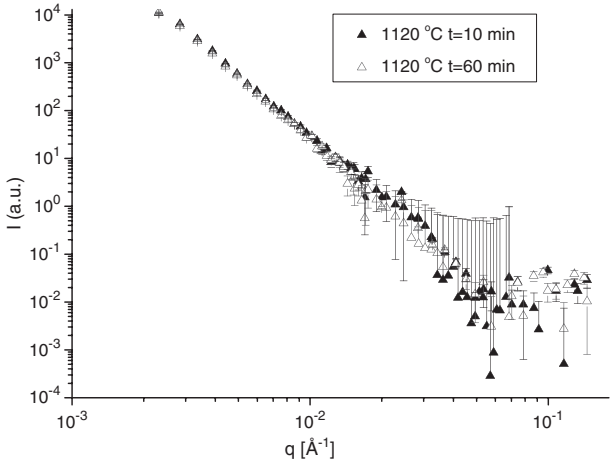

Figure 4. Scattered intensity plotted as a function of q at two different ageing times.

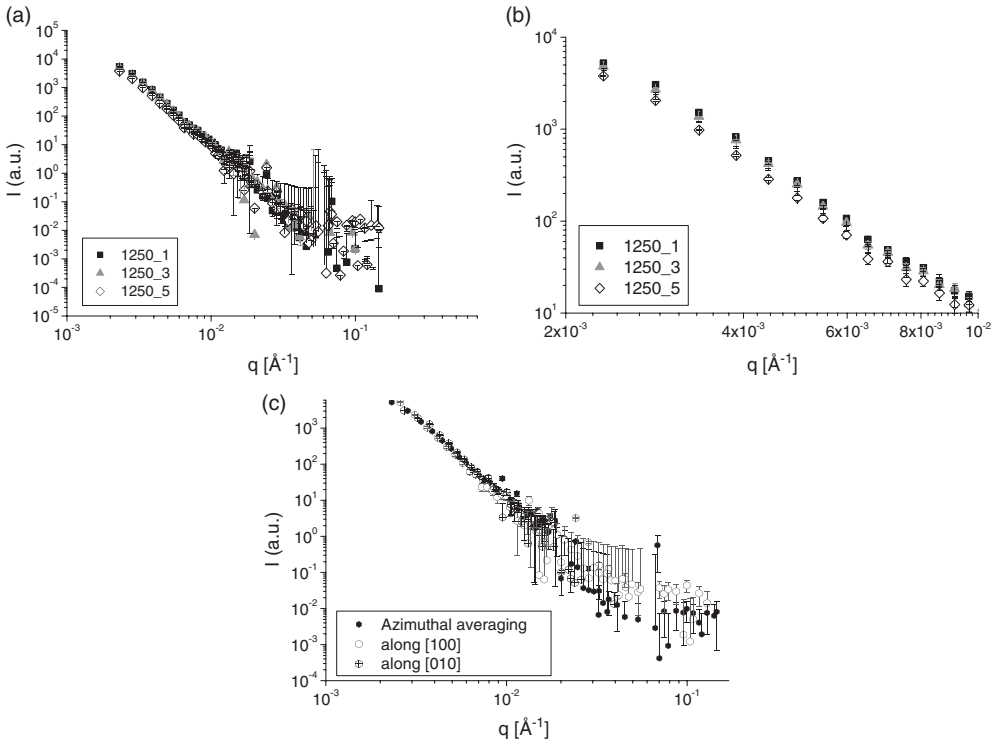

Figure 5. (a) Scattered intensity plotted versus q for the successive dissolutions at 1250 °C. (b) Zoom of (a) in the low-q domain. (c) Scattered intensity versus q for the different directional analyses at 1250 °C. No evolution in the SANS signal is visible, which confirms the isotropic characteristic of the signal.

as a function of time was noticeable at any temperature. A total isothermal SANS intensity was then calculated by summing up all the scattering data obtained at each temperature T.

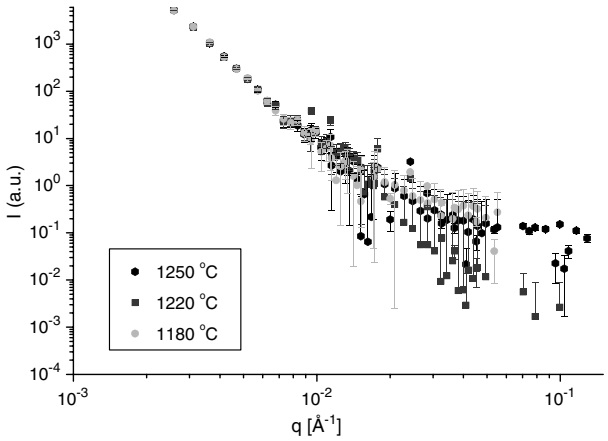

Figure 6. Scattered intensity in the case of isotropic SANS patterns.

Figure 5(a) shows the scattered intensity plotted as a function of q (Å^{-1}) for some of the successive solutionizing treatments of the γ' precipitates, with a double-logarithmic scale. The asymptotic behaviour of the scattered intensity is q^{-4} which, combined with the isotropic character of the signal (see figure 5(c)), reveals the presence of spherical particles remaining even after solutionizing [15]. Their contribution to the scattering pattern is visible either outside or in the low-q region of the investigated q-range.

This is confirmed by the fact that the scattered intensity exhibits a deviation from the q^{-4} law behaviour at low q-values. This would correspond to the 'Guinier' contribution from a distribution of relatively big precipitates [24] of roughly 500 nm size. As shown in figure 5(b), this contribution tends to decrease through the successive solutionizing treatments. This could indicate that the volume fraction of these big spherical particles tends to slightly decrease through the successive dissolutions. The SANS signal at high q-values contains a contribution of the incoherent scattering, which increases the error bars in the high-q domain.

The $I(q)$ curves at 1220 and 1180 °C do not differ substantially from that at 1250 °C, as shown in figure 6, except for a slight increase of the signal at 1180 °C in the high-q region. This means that the microstructure does not evolve throughout these ageing processes and only around 1180 °C are small particles with size from 1 to 5 nm nucleated, as deduced from the above-mentioned Guinier contribution. At temperatures below 1180 °C (1120, 1050, 860 °C and RT before the different ageing) the scattered intensity increases with decreasing temperature, as shown in figures 7(a)–(d) (the profile at RT after the ageing treatments essentially coincides with that before the heat exposure and therefore is omitted). As pointed out earlier, the 2D pattern becomes anisotropic. This is also visible comparing figures 8 and 9 with figures 7 and 10. It implies the presence of non-spherical (cuboidal) objects aligned along the {100} faces.

4. Analysis

4.1. Anisotropy

A model was developed so as to know what kind of information the different directional averages contain with respect to the shape of the precipitates. We assume that our system is composed of two types of γ' precipitates: the first with a spherical shape (as some spherical

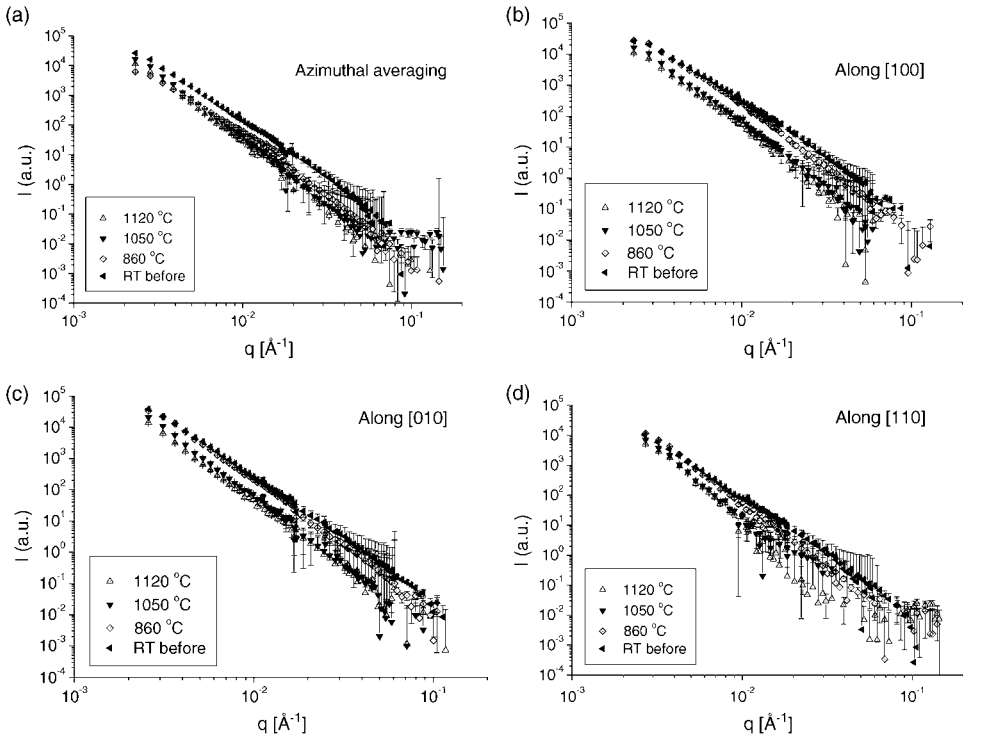

Figure 7. (a) Scattered intensity evolution as a function of temperature in the case of an azimuthal averaging; (b) in the case of an averaging along the [100] crystallographic direction; (c) in the case of an averaging along the ⟨010⟩ crystallographic direction; (d) in the case of an averaging along the ⟨110⟩ crystallographic direction.

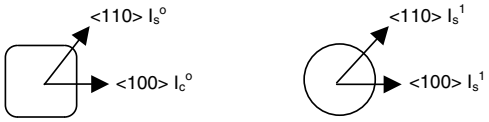

Figure 8. Contributions to the scattered intensity depending on the particles shape (cuboidal or spherical) and the crystallographic direction of analysis.

particles remain at high temperatures) and the second with a cuboidal shape. It is also assumed that the cuboidal particles are perfectly aligned along the $\{100\}$ directions but with rounded corners, exhibiting then a spherical shape along the $\{110\}$ crystallographic directions, as shown in figure 8. Therefore, the scattered intensity averaged along the [110] direction $I_{\langle 110\rangle}$ is the sum of the two contributions with spherical form factors coming from the scattering of both cuboidal (labelled I_s^0) and spherical particles (labelled I_s^1). In the same way, the scattered intensity averaged along the [100] direction $I_{\langle 100\rangle}$ is the sum of two contributions: one with a spherical form factor coming from the scattering of spherical particles (which is always I_s^1) and the second with a cubic form factor coming from the scattering of cuboidal particles (noted I_c^0). The azimuthally averaged scattered intensity is the sum of all contributions.

$$I_{az} = I_c^0 + I_s^0 + I_s^1 \tag{2}$$

$$I_{\langle 100\rangle} = I_c^0 + I_s^1 \tag{3}$$

$$I_{\langle 110\rangle} = I_s^0 + I_s^1. \tag{4}$$

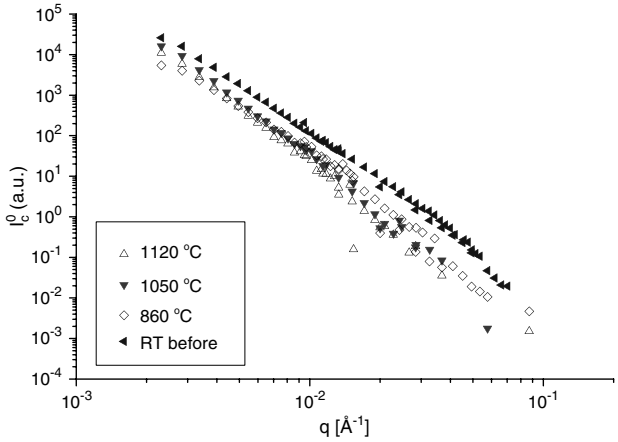

Figure 9. Evolution of I_c^0 as a function of temperature.

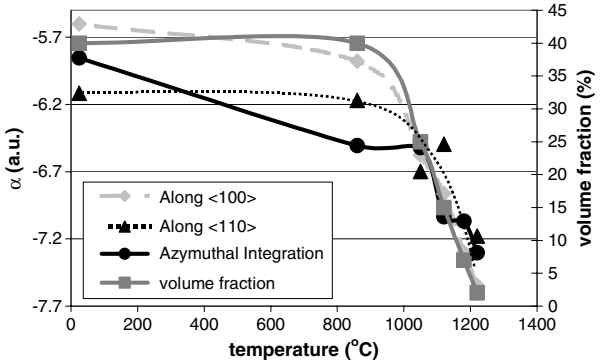

Figure 10. q^{-4} scattered intensity and volume fraction as measured in [5] as a function of temperature.

Thus,

$$I_{\mathrm{az}} - I_{\langle 110\rangle} = I_{\mathrm{c}}^0. \tag{5}$$

We also note that this approach contains inherently the volume fractions of the particle types.

Using this model, we can isolate the contribution to the SANS signal from cuboidal precipitates (see figure 9 based on equation (5)).

At temperatures below 1120 °C we find an increase of the SANS signal coming from cuboidal precipitates, which is consistent with an increasing volume fraction of them, as expected and previously mentioned. In addition, the cuboidal component of the scattered intensity shows a decrease at low q-values at 860 °C accompanied with a corresponding increase in scattered intensity at higher q-values. This phenomenon implies an unexpected size decrease of the cuboids and will be discussed later.

4.2. Evolution of the relative scattered intensity with ageing temperature

In order to get a better observation of the changes in the microstructure due to ageing, the SANS signals obtained at temperatures below 1220 °C are compared relatively to that obtained

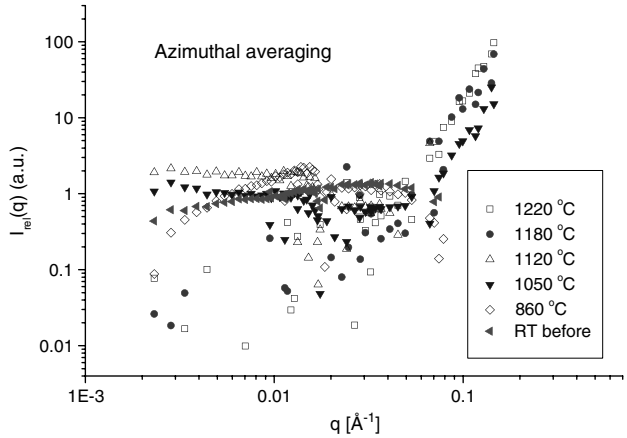

Figure 11. Evolution of the relative scattered intensity azimuthally averaged with temperature.

at 1250 °C, where some particles still remain, as mentioned earlier. Furthermore, the q^{-4} contribution can be also removed so as to separate the contribution from distributions of particles truly belonging to the investigated q-range and big particles yielding their 'Porod' signal in this range. We thus define:

$$I_{\mathrm{rel}}(T,q) = \frac{I(T,q) - I(T = 1250\,^{\circ}\mathrm{C}, q)}{\alpha(T) \cdot q^{-4}} \qquad T \leqslant 1250\,^{\circ}\mathrm{C} \tag{6}$$

where $\alpha(T) = I(T, q = 1) - I(T = 1250\,^{\circ}\mathrm{C}, q = 1)$ is defined as the q^{-4} 'offset' of the scattered intensity and represents the asymptotic contribution of big particles (with size bigger than 800–1000 nm). By means of equation (6) we then calculate the fluctuations of the SANS signals due to the evolution of the populations of particles through the ageing processes. It is to be noted that the choice of $q = 1$ for the definition of α is arbitrary and does not affect the relative values of $\alpha(T)$.

Figure 10 shows the evolution of α as a function of temperature, compared with the experimental volume fraction determined in [5]. It is clearly seen that the value of α increases with decreasing temperature, which is consistent with an increase in the γ' volume fraction. Moreover, the increase of α is more pronounced if we integrate the 2D pattern in sectors centred along the [100] and the [010] crystallographic directions than along the [110]. This implies an increase in the particle order along the [100] and [010] crystallographic directions.

Figure 11 shows the relative intensity $I_{\mathrm{rel}}(q)$, as azimuthally averaged at each temperature. $I_{\mathrm{rel}}(q)$ increases in the high-q range between 1220 and 1050 °C, which possibly indicates that small spherical particles are nucleated at high temperature, with very small size (10–25 nm). At 1120 °C and below, the relative intensity $I_{\mathrm{rel}}(q)$ is constant in the intermediate- and low-q range (but noticeably larger than at 1180 °C). At 860 °C and RT the behaviour is different, because the signal is smaller than at 1120 °C, and increases as a function of q. $I_{\mathrm{rel}}(q)$ seems to be larger at 1120 °C than at lower temperatures, while at large q the tendency is reversed. This implies that the very small particles nucleated at high temperatures increase their size, but upon cooling, further nucleation takes place.

As seen in figure 12, there is a strong decrease in the scattered intensity I_{c}^{0} at low q between 1050 and 860 °C. While at 1050 °C a 'peak' is observed at low q-values, corresponding to a distribution of relatively big cuboidal particles (approximate size of 200 nm), this disappears at 860 °C and 'pops up' in the intermediate-q region (size around 50 nm). This indicates that

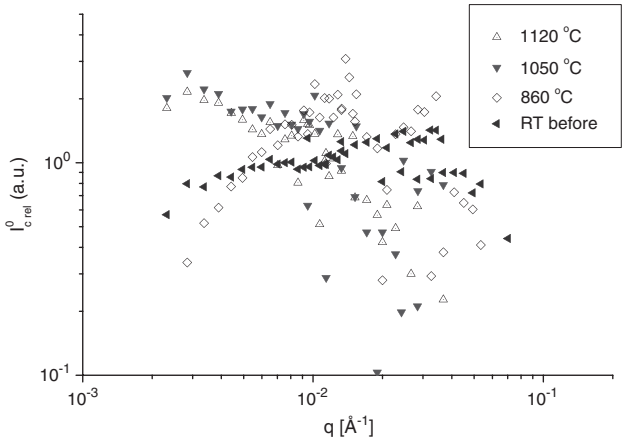

Figure 12. Relative scattered intensity $I^0_{c,rel}$.

Table 3. γ' volume fraction evolution with temperature [5, 27].

Temperature (°C)	1250	1220	1180	1120	1050	860	25
Volume fraction (%)	1	2	7	15	25	40	40

the volume fraction of these big cuboidal particles is decreased and, if we take into account the particle size ratio 4:1, gives hints that some splitting of big precipitates into smaller particles takes place.

4.3. Data modelling

The SANS data $I(T, q)$ were modelled so as to obtain quantitative information about the γ' particle populations coexisting at each temperature. The analysis was carried out on the azimuthally averaged data. Therefore, we assumed that polydisperse spherical and cuboidal particle populations could have the same (spherical) form factor in the temperature and q-ranges considered. Although this may seem a drastic approximation, the systematic error introduced by the assumption that the *averaged* form factor of cubic particles is that of spherical particles has been shown to be below the usual experimental errors of SANS measurements [25].

Three populations of polydisperse spherical particles were necessary to model the experimental results. The scattered intensity was calculated using the following equations:

$$\frac{\mathrm{d}\Sigma}{\mathrm{d}\Omega}(q) = n_p \cdot \langle |F(q)|^2 \rangle \tag{7}$$

$$\langle |F(q)|^2 \rangle = \int_0^\infty |F(q, R)|^2 f(R)\,\mathrm{d}R \tag{8}$$

where $F(q, R)$ is the form factor for a sphere of radius R [25], $n_p = N_p/V$ is the average number density of particles in the sample and $f(R)$ the particle size distribution, which is modelled. In our case, $f(R)$ is a Schultz distribution, as defined in [26]. In view of the low γ' volume fraction, the interaction between particles was not considered. The evolution of the γ' volume fraction with temperature found in [5, 27] was taken into account (see table 3 and figure 10). The characteristic parameters of the three populations of particles used to model the scattered intensity are shown in table 4, and the match between data and model in figures 13(a)–(f).

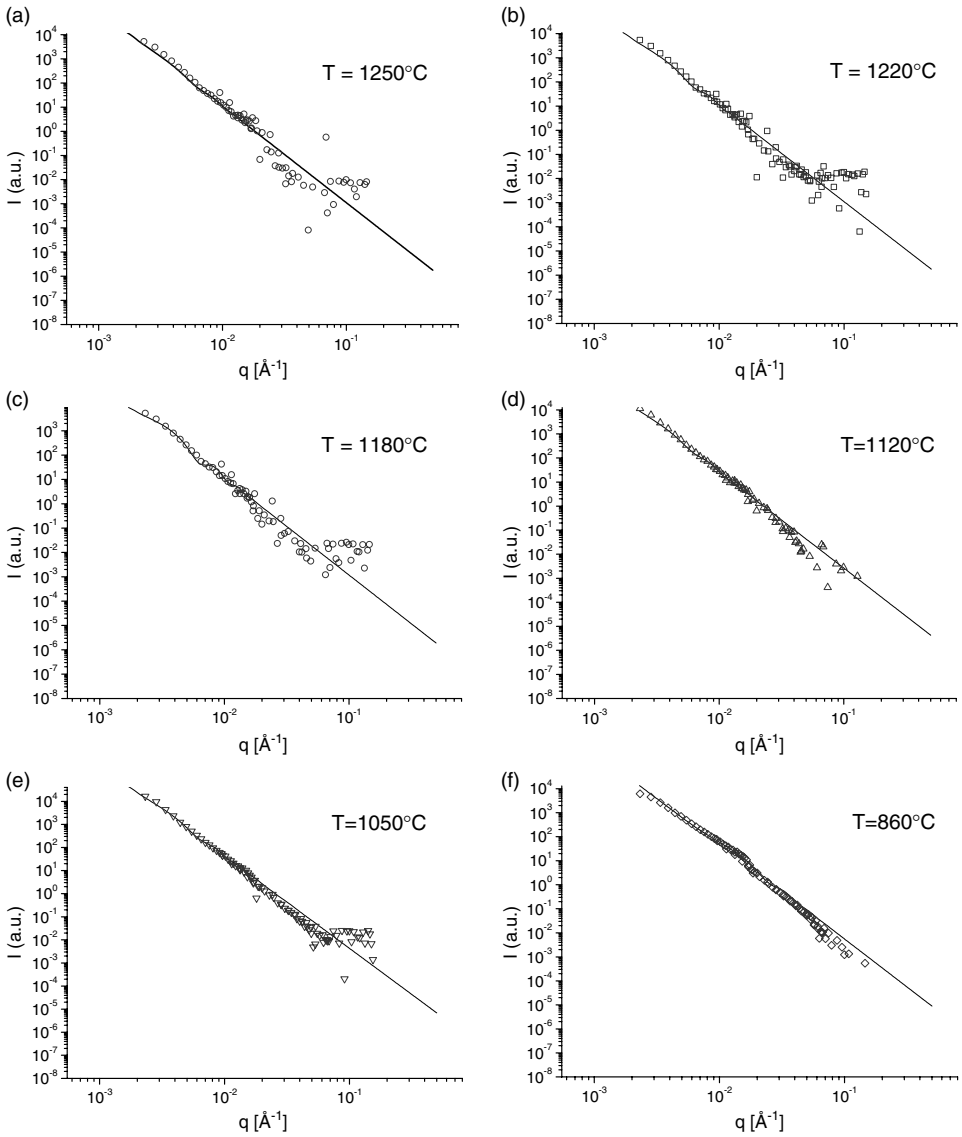

Figure 13. (a)–(f): Model (line) and experimental (dots) scattered intensities at all temperatures. The agreement between model and data is good, as the model reproduces the main features of the data profile.

At each temperature, the contribution (to the total intensity) of a population of particles is multiplied by a weight corresponding to the fraction of γ' particles belonging to this population (see table 4). The total theoretical intensity is the sum of the three weighted contributions of each population. The model data show a good agreement with the experimental data.

Figure 14 shows the evolution of the modelled particle sizes and volume fractions. The 'large' particles represented by population 1 remain throughout the whole ageing processes but in low volume fraction (about 0.1%). The volume fraction of medium-size particles (population 2) first increases between 1250 and 1180 °C but then decreases below 1050 °C, being replaced

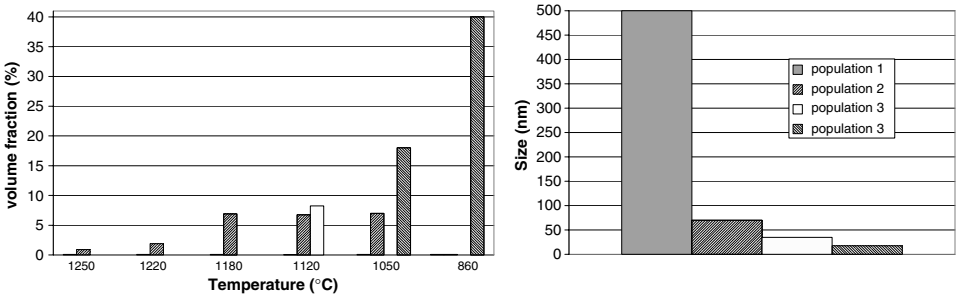

Figure 14. Size (radius) and volume fraction of the different modelled particle populations.

Table 4. Definition of the populations used for the modelling. R is the mean radius of the Schultz distribution and Z the width term. The volume fractions (weights) used at each temperature are shown.

			Relative volume fraction (%)					
	R (nm)	Z	1250 °C	1220 °C	1180 °C	1120 °C	1050 °C	860 °C
Population 1	500	50	0.1	0.1	0.1	0.1	0.1	0.1
Population 2	70	100	1	2	7	7	7	0.1
Population 3	35	75	0	0	0	9	0	0
Population 3′	17.5	75	0	0	0	0	18	40

by smaller particles (population 3 (around 1120 °C) and population 3′ (below 860 °C)). The fraction of population 2 remaining at 860 °C is relatively low.

From figure 13, it is clearly shown how the model can reproduce the main features of the $I(q)$ curves at every temperature. Under the present conditions (many polydisperse populations), it is not viable to attempt fitting the data, as for instance was done by Schneider *et al* [28]. There are several reasons for preferring a simple model.

(1) In absence of a Guinier signal (i.e., first interference fringes at low q), the volume fraction and the particle size (i.e., the position of the distribution in the q-range) are strongly coupled and every fitting routine becomes unstable.
(2) If a population of big particles is present, essentially resulting in a q^{-4} signal in the observable range of q, its signal will basically cover all other contributions, even if its volume fraction is very low. This causes wide variations of the parameters characterizing other populations, since a local minimum is always reached in the parameter space. This implies that the fitting parameters of the distributions of medium- and low-size particles lie on a saddle point for the χ^2 function.
(3) The number of parameters to fit is too large, even if three populations are assumed, especially if cubic and spherical particle form factors are taken into account.

5. Discussion

The observations made in figures 7(a)–(d) indicate the appearance of an increasing γ' volume fraction of particles between 1120 and 860 °C (a rising SANS signal in the investigated q-range). In this temperature range, figures 9,11,12 show, as a function of decreasing temperature, a decrease of the SANS intensity in the low-q region and an increase in the high-q region. The high-q SANS intensity increase is certainly due to newly nucleated particles but the splitting of

big existing particles into smaller ones cannot be excluded, since nucleation is expected to be very low at temperatures below 1000 °C and decreases with decreasing temperature. The low-q SANS intensity decrease confirms this hypothesis, as one would expect particle coarsening and therefore an increasing SANS signal in the low-q region. Therefore, it is reasonable to think that the influence of particles splitting on the SANS signal is of the same order as that caused by the nucleation of new particles, combined with a decrease in volume fraction of big particles. This renders the distinction between the two phenomena difficult.

According to the mentioned theoretical works of Khachaturyan [8, 9], above a critical precipitate size the elastic strain energy prevails over the particle/matrix interfacial energy, equation (1), and leads to a morphological shape transition: the big particles split into smaller according to the model cube → doublet → octet [9] (a phenomenon driven by the elastic anisotropy). These calculations are based on the final precipitates' arrangements without taking into account the transition states. Also, in work of Colin *et al* [29] the possibility of splitting is shown to be energetically favourable, although an 'activation' energy or a crack in the γ' particle is needed to start the splitting. Another explanation for the driving mechanism of splitting could be the fluctuations from the equilibrium state in terms of chemical composition at the interface between matrix and particles [10], thus enhancing the diffusion processes responsible for particle splitting.

The modelling done in the present work is in full agreement with the splitting hypothesis as the mean size of population 2 is twice the size of population 3 and four times the mean size of population 3′ (as shown in figure 14). The transition from cube to doublet could then occur around 1120 °C, followed by the transition from doublet to octet around 1050 °C. Very few particles belonging to population 2 remain at 860 °C, once the splitting is achieved (see figure 14).

According to this, a possible scenario for the γ' precipitation sequence can be drawn. For temperatures higher than 1120 °C, the γ' phase is distributed into two populations of spherical particles randomly distributed within the matrix. The bigger precipitates tend to coarsen at the expense of smaller ones so as to reduce the total interface area between the matrix and the precipitates, which reduces the interfacial energy. Between $T = 1180$ and 1120 °C, under the effect of the anisotropic elasticity, the precipitates change shape and become cube-like. In addition, the elastic forces due to the lattice mismatch and the elastic anisotropy tend to align the precipitates along the elastically soft direction, $\{100\}$. These changes in microstructure are consistent with the findings of previous diffraction works [5], where the strain relaxation rate was found to be maximum at about 1120 °C. A second transition occurs around 1050 °C where the splitting phenomenon seems to take over. Indeed, previous synchrotron radiation diffraction *in situ* experiments [30] identified 1050 °C as the transition temperature where the total reaction rate has a maximum.

6. Conclusions

The microstructural evolution of the γ' reinforcing phase in the SC16 nickel-based single-crystal superalloy was monitored *in situ* using small-angle neutron scattering. After a solutionizing treatment at 1250 °C, the alloy was held at different temperatures. Essentially, no time evolution could be observed during each isothermal treatment. The SANS intensity was referred to that collected at 1250 °C, which was found to carry the footprints of the presence of large undissolved particles.

A data modelling was done, assuming azimuthal average, and was found to be in good agreement with the observed data.

The following conclusions could then be drawn from the analysis and the modelling.

At high temperatures, just below the *solvus* point (from 1220 to 1180 °C) small spherical particles are nucleated. Nucleation continues taking place down to 1050 °C. The particles tend to grow and to become cuboidal around 1120 °C. Their size tends to increase up to about 200 nm and then to decrease in the observable q-range. This implies that concurrent phenomena of growth of very big particles (>500 nm), contributing to the SANS intensity with an increasing q^{-4} signal, and particle splitting into doublets and then octets occur.

Acknowledgments

We would like to acknowledge the ILL for provision of beamtime on D11. H Cavalcanti Pinto (T U Wien) and Robert Cubitt (ILL) were part of the experimental team and are thanked for their assistance. We also thank Charles Dewhurst (ILL) for his assistance during the data analysis.

References

[1] Durand-Charre M 1997 *The Microstructure of Superalloys* (Amsterdam: Gordon and Breach Science) ISBN 90-5699-097-7
[2] Murakamo T, Kobayashi T, Koizumi Y and Harada H 2004 *Acta Mater.* **52** 3737–44
[3] Hornbogen E and Warlimont H 1991 *Metallkunde, Aufbau und Eigenschaften von Metallen und Legierungen* (Berlin: Springer) pp 134–44
[4] Cahn J W 1959 *Acta Metall.* **7** 18
[5] Bruno G and Pinto H C 2003 *Mater. Sci. Technol.* **19** 1–6
[6] Lifshitz I M and Slyozov V V 1961 *J. Phys. Chem. Solids* **19** 35–50
[7] Wagner C 1961 *Z. Elektroch.* **65** 581–91
[8] Khachaturyan A G 1983 *Theory of Structural Transformation in Solids* (New York: Wiley)
[9] Khachaturyan A G, Semenovskaya S V and Morris J W Jr 1988 *Acta Metall.* **36** 1563–71
[10] Yamabe-Mitarai Y and Harada H 2002 *Phil. Mag. Lett.* **82** 109–18
[11] Hopgood A A and Martin J W 1986 *Mater. Sci. Technol.* **2** 543–8
[12] Royer A, Bastie P and Veron M 1998 *Acta Mater.* **46** 5357–68
[13] Strunz P, Mukherji D, Gilles R, Wiedenmann A, Rösler J and Fuess H 2001 *J. Appl. Crystallogr.* **34** 541–8
[14] Malow T, Zhu J and Wahi R P 1994 *Z. Metallk.* **85** 9–18
[15] Malow T 1993 *Diplomarbeit* TU Berlin
[16] Gilles R, Mukherji D, Strunz P, Wiedenmann A and Wahi R P 1997 *Z. Metallk.* **88** 518–21
[17] Gilles R, Mukherji D, Strunz P, Lieske S, Wiedenmann A and Wahi R P 1998 *Scr. Mater.* **39** 715–21
[18] Ricks R A, Porter A J and Ecob R C 1983 *Acta Metall.* **31** 43–53
[19] Westbrook J H 1958 *Z. Kristallogr.* **110** 21–9
[20] Kostorz G 1991 *J. Appl. Crystallogr.* **24** 444–56
[21] http://www.ill.fr/lss/grasp/grasp_main.html
[22] Bellet D, Bastie P, Royer A, Lajzerowicz J, Legrand J F and Bonnet R 1992 *J. Physique* I **2** 205–20
[23] Strunz P, Mukherji D, Gilles R, Wiedenmann A and Fuessd H 2001 *J. Appl. Crystallogr.* **34** 541–8
[24] Guinier A 1964 *Théorie et technique de la radiocristallographie* 3rd edn (Paris: Dunod) chapter XIV p 637
[25] Cernuschi F and Fiori F 1997 ENEL/CRAM-University of Ancona, C.R. R25VC0105/00
[26] Kotlarchyk M and Chen S H 1983 *J. Chem. Phys.* **79** 2461–9
[27] Bruno G, Pinto H C and Reimers W 2002 *Appl. Phys.* A **74** S940–2
[28] Schneider J-M, Schönfeld B, Demé B and Kostorz G 2000 *J. Appl. Crystallogr.* **33** 465–8
[29] Colin J, Grilhé J and Junqua N 1998 *Acta Mater.* **46** 1249–55
[30] Pinto H C and Bruno G 2003 *J. Synchrotron. Radiat.* **10** 148–53